Flow past a plate in the vicinity of a free surface

Article *in* Ocean Engineering · January 2016

DOI: 10.1016/j.oceaneng.2015.11.009

4 authors:

I-Han Liu
Lehigh University
4 PUBLICATIONS **7** CITATIONS
SEE PROFILE

Jacob Riglin
Lehigh University
19 PUBLICATIONS **92** CITATIONS
SEE PROFILE

William Schleicher
Lehigh University
19 PUBLICATIONS **93** CITATIONS
SEE PROFILE

Alparslan Oztekin
Lehigh University
104 PUBLICATIONS **850** CITATIONS
SEE PROFILE

Ocean Engineering 111 (2016) 323–334

Contents lists available at ScienceDirect

Ocean Engineering

journal homepage: www.elsevier.com/locate/oceaneng

Flow past a plate in the vicinity of a free surface

I-Han Liu, Jacob Riglin, W. Chris Schleicher, Alparslan Oztekin *

Mechanical Engineering and Mechanics, P.C. Rossin School of Engineering and Applied Science, Lehigh University, Bethlehem, PA 18015, USA

ARTICLE INFO

Article history:
Received 24 January 2015
Accepted 13 November 2015

Keywords:
Marine energy
Free surface
Computational fluid mechanics
Drag coefficient

ABSTRACT

Two-dimensional transient simulations are performed to investigate characteristics of flow past a plate normal to a stream. Free surface effects on the flow dynamics are the primary focus of this study. Varying plate depths are simulated to examine the variation of force coefficients and vortex shedding patterns. The k–ω Shear Stress Transport (k–ω SST) turbulence model and Volume of fluid (VOF) multiphase model are employed to predict characteristics of free surface flow. Flow past the plates is simulated at distances of 0.75 m, 0.06 m, 0.05 m, 0.045 m, and 0.03 m below the free surface with corresponding local Froude numbers (Fr) of 0.18, 0.65, 0.71, 0.75, and 0.92. As the plate gets closer to the surface the drag coefficient decreases from 3.86 (Fr=0.18) to 2.18 (Fr=0.92) and the Strouhal number increases from 0.125 (Fr=0.18) to 0.355 (Fr=0.92). A jet-like flow formed from the surface is observed on top of the plate. Vortices from the top surface of the plate dissipate into smaller eddies due to the free surface presence, resulting in asymmetric vortex shedding downstream. Flows presented here are beneficial for designing and optimizing systems that harvest energy from marine currents.

1. Introduction

Proper numerical simulations are a valuable proxy for studying fluid flow characteristics while minimizing costly experiments. Understanding the flow around a rectangular bluff body is of practical importance in various fields of engineering. Structures such as bridge decks, platforms, offshore pipelines, and hydropower systems often interact with the free surface. The normal rectangular prism is a simple geometry used to understand complex phenomena such as flow separation, wake instabilities, the unsteady vortex shedding formation, and the force acting on the cylinder. Estimating structural hydrodynamic forces is an important design consideration for offshore structures under unsteady flow conditions. Hydrokinetic turbines for river current applications typically operate near surfaces and the effect of the free surface on the performance of these energy harvesting devices could be profound.

Hydrokinetic power is an alternative clean energy source to conventional power such as fossil fuels and nuclear power. Hydrokinetic turbines have been studied by various research groups; however, these engineering designs are limited by water depth. In general, the blades are placed perpendicular to the flow path in order to extract the energy from rivers. A single flat plate submerged at different water depths is investigated as a preliminary study for marine current systems, where the power extracted is directly proportional to the drag force exerted on the blades. Maximizing the drag force is therefore equivalent to maximizing the power extracted. The free surface effect is studied to determine a proper plate depth so sufficient power can be generated while the hydropower system is operated near the free surface.

Free surface flows are challenging hydraulic engineering scenarios. For instance, when a cylinder is placed closer to the free surface, the forces acting on the cylinder become increasingly complicated due to the interaction between the free surface and the cylinder. Also, the wake behind structures and water surface deformation are altered in such free surface scenarios as well. Several researchers approached this problem numerically (Miyata et al., 1990; Arslan et al., 2013) and experimentally (Miyata et al., 1990; Sheridan et al., 1997; Reichl et al., 2005; Malavasi and Guadagnini, 2007; Negri et al., 2010; Arslan et al., 2013) by employing circular or rectangular cylinders.

Generally, hydrodynamic forces acting on the object decreased when the object is closer to the surface, as described in Miyata et al. (1990) and Malavasi and Guadagnini (2007). A simultaneously occurring abrupt drop in drag coefficient and increase in Strouhal number is reported by Miyata et al. (1990) when the depth–radius ratio was down to 1.7. Malavasi and Guadagnini (2007) experimentally investigated a rectangular cylinder submerged in a water channel at various depths. They found that the drag coefficient decreases drastically and Strouhal number

* Corresponding author. Tel.: +1 610 758 4343.
E-mail address: alo2@lehigh.edu (A. Oztekin).

http://dx.doi.org/10.1016/j.oceaneng.2015.11.009
0029-8018/

Nomenclature

A	cross sectional area
a, a_1	closure coefficient
B	channel width
C	courant number
C_D	drag coefficient
C_L	lift coefficient
d	plate depth
d^*	dimensionless plate depth
f	vortex shedding frequency
F_D	drag force
F_L	lift force
Fr	Froude number
F_1, F_2	blending functions
g	gravity
GCI	grid convergence index
h	water depth
h_b	cylinder elevation above channel floor
h^*	$(h- h_b)/ s$, non-dimensional depth
k	turbulent kinetic energy
l	cylinder cross-section length
L	plate height
$\dot{m}_{12}$, $\dot{m}_{21}$	mass transfer between phase 1 and 2
N_1, N_2, N_3	number of cells
P	pressure
Re	Reynolds number
s	cylinder cross-section width
S	mean rate-of-strain tensor
t	time
Δt	time step size
u_i, u_j	velocity in tensor notation
u_*	friction velocity at the nearest wall
U_∞	water velocity
U_{air}	air velocity
U_f	volume flux through the face based on normal velocity
V	volume of cell
$\forall_{air}$	volume of air within the cell
$\forall_{cell}$	volume of a cell
$\forall_{water}$	volume of water within the cell
$\mathbf{V}$	upstream water velocity
w	plate width
x_i	position vector in tensor notation
Δx	grid width
y	distance to the nearest wall
y^+	dimensionless wall distance

Greek Symbols

α	volume fraction
β, β^*	closure coefficient
δ_{ij}	Kronecker delta
μ	dynamic viscosity
ν	kinematic viscosity
ν_T	eddy viscosity
ρ	density
$\sigma_k, \sigma_\omega,\ \sigma_{\omega 2}$	closure coefficients
τ_{ij}	stress tensor
ω	specific dissipation rate
Ω	vorticity magnitude

increases with decreasing depth of the cylinder. Both Miyata et al. (1990) and Sheridan et al. (1997) studied the wake structure of flow past a circular cylinder close to the free surface. The presence of the cylinder, which caused the formation of surface waves, altered the dynamics of the free surface and produced a jet-like flow near the free surface. When the cylinder was shallowly submerged, the free surface distortion and asymmetric vortex shedding from the cylinder occurred. Such asymmetric vortex shedding resulted in intense turbulent fluctuations due to the flow confinement on top. Negri et al. (2010) applied a self-synchronized phase averaging technique to PIV velocity fields to study flow past a rectangular cylinder near a free surface. The vortex shedding process and the wake evolution were reported by employing the phase-averaged flow fields. Another study on the free surface deformation and wake behavior with respect to Froude number is presented in Reichl et al. (2005). Results of two-dimensional simulations showed that the surface deformation was sensitive to the Froude number. The surface deformation and the intensity of surface waves became substantial as the Froude number increased from 0.35 to 0.40. Arslan et al. (2013) investigated the flow field of partially submerged rectangular cylinder by conducting large eddy simulations and experimental measurements. They concluded that the magnitude of the drag force is very sensitive to the submergence ratio.

Flow past bluff bodies in an infinite fluid domain has been widely studied both experimentally and numerically. Simple geometries such as circular cylinders, rectangular prisms, and flat plates have been investigated to understand the vortex dynamics and the drag and lift forces. Fage and Johansen (1927) experimentally measured the upstream and downstream pressures for an inclined flat plate with

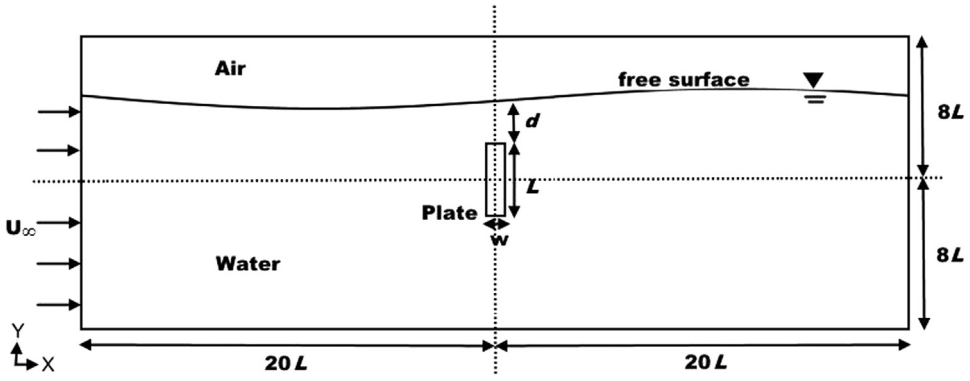

Fig. 1. The schematic of the flow geometry.

various angles of attack. Knisely (1990) experimentally studied the Strouhal numbers for rectangular prisms with various aspect ratios at different angles of attack. Both Narasimhamurthy and Andersson (2009) and Najjar and Vanka (1995) numerically studied the structure and dynamics of the wake flow behind the flat plate. Simulations were carried out for low Reynolds number and the mean drag and pressure coefficients were reported as well. In a recent work, Tian et al. (2013) investigated the effect of aspect ratio for two-dimensional flow around rectangular prisms by conducting numerical simulations using the k–ω SST turbulence model. Bayraktar et al. (2014) conducted simulations for flow past circular, square, and diamond cylinders in the proximity of no-slip wall. Results revealed that the flow pattern loses periodicity as the gap between the cylinder and the wall becomes smaller. Bayraktar et al. (2014) also documented that the mean value of drag coefficient decreased substantially as the cylinder is placed near the wall.

In spite of extensive studies on flow past bluff bodies, the understanding of the free surface effect is still limited when a near-surface object is interacting with the free surface. Investigating the effect of the free surface on the flow dynamics is the primary objective of this manuscript. The presence of the free surface affects both force coefficients and the wake structure behind the object. In the present study, two-dimensional numerical simulations are carried out to investigate the change of flow field and hydrodynamic forces on the normal plate as the plate depth is varied. A three-dimensional validation simulation was conducted to compare with the experimental results provided by Malavasi and Guadagnini (2007). The flow pattern, drag and lift coefficients, and the Strouhal number as a function of plate depth (Froude number) are reported in this paper. The present study will aid the design of a hydropower system for river and ocean current applications.

2. Mathematical model

The two-dimensional transient simulation is regarded as an infinitely long prism immersed in the flow. The basic flow physics and the hydrodynamic forces exerted on the submerged object are investigated by conducting such simulations. The VOF method models two immiscible fluids by solving mass and momentum conservation equations. The volume fraction for each fluid in cells can be tracked throughout the domain. The air volume fraction is defined by a scalar function α, which is the volume of air divided by the volume of the local cell. Volume fraction is bounded between $0 \le \alpha \le 1$, corresponding to water-filled cells and air-filled cells, respectively. When $0 < \alpha < 1$, the cell contains the interface between air and water. α is expressed as

$$\alpha = \frac{\forall_{air}}{\forall_{cell}} = \frac{\forall_{air}}{\forall_{air} + \forall_{water}} \tag{1}$$

where $\forall_{cell}$ is the volume of a cell, $\forall_{air}$ is the volume of air within the cell, and $\forall_{water}$ is the volume of the water within the cell. The mass and momentum equations for multiphase flow are written as (see Hirt and Nichols, 1981; Monaghan, 1994)

$$\frac{\partial u_i}{\partial x_i} = 0 \tag{2}$$

$$\frac{\partial}{\partial t}(\rho u_i) + \frac{\partial}{\partial x_j}(\rho u_j u_i) = -\frac{\partial P}{\partial x_i} + \frac{\partial}{\partial x_j}\left[\mu\left(\frac{\partial u_j}{\partial x_i} + \frac{\partial u_i}{\partial x_j}\right)\right] + \rho g_i \tag{3}$$

where u_i is the velocity, ρ is the density, μ is the dynamic viscosity, P is the pressure, and g is the gravity. The density of the mixture is defined in terms of α as

$$\rho = \alpha\rho_1 + (1-\alpha)\rho_2 \tag{4}$$

where ρ_1 denotes the density of the primary phase (air) and ρ_2 denotes the density of the secondary phase (water). Interface tracking between water and air is accomplished by solving the continuity equation for the phase's volume fraction, which has the following form:

$$\frac{\partial}{\partial t}(\alpha\rho_1) + \frac{\partial}{\partial x_i}(\alpha\rho_1 u_1) = \dot{m}_{21} - \dot{m}_{12} \tag{5}$$

where u_1 represents the velocity of the primary phase and $\dot{m}_{21}$ and $\dot{m}_{12}$ are the mass transfers between air and water. The plate is set to be perpendicular to the streamwise direction. The upstream water speed, U_∞, is the relative fluid speed with respect to the plate.

In order to find out how much energy can be extracted, the force acting on the plate must be determined. The drag and lift coefficients (C_D and C_L) are defined as

$$C_D = \frac{F_D}{\frac{1}{2}\rho {U_\infty}^2 A},\ C_L = \frac{F_L}{\frac{1}{2}\rho {U_\infty}^2 A} \tag{6}$$

where F_D is the drag force, F_L is the lift force, and A is the area of the immersed object projected over the incoming flow.

The Reynolds number is based on the upstream water velocity U_∞ and the plate height L. It is calculated as $Re_2 = \rho_2 U_\infty L/\mu_2$ where μ_2 is the water dynamic viscosity. Strouhal number,

Table 1
Parameter values used in the simulations.

Parameter values					
A	0.1	[m^2]	U_{air}	0.01	[$m\ s^{-1}$]
g	9.81	[$m\ s^{-2}$]	U_∞	0.5	[$m\ s^{-1}$]
L	0.1	[m]	w	0.01	[m]
d	0.75,0.06, 0.03	[m]	ρ_2	1000	[$kg\ m^{-3}$]
Re_2	50,000	[dimensionless]	μ_2	0.001	[$kg\ m^{-1}\ s^{-1}$]

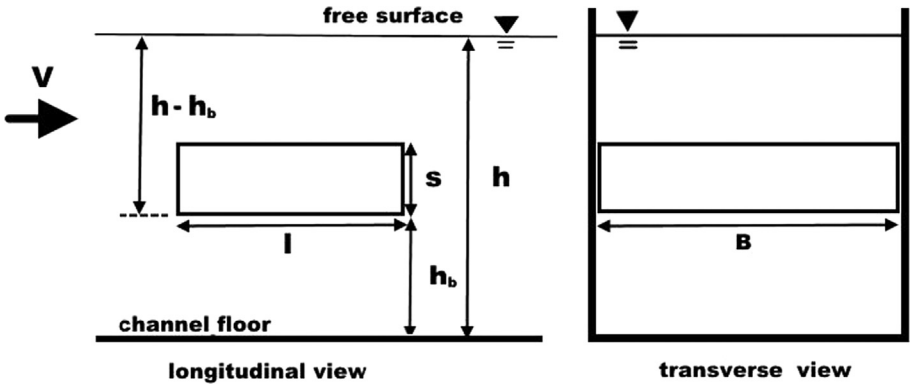

Fig. 2. Geometry of the validation simulation.

Table 2
Parameter values used in the validation simulation.

Parameter values		
l	0.18	[m]
s	0.06	[m]
h	0.3798	[m]
h_b	0.1398	[m]
h^*	4	[dimensionless]
B	0.5	[m]
V	0.334	[m s^{-1}]

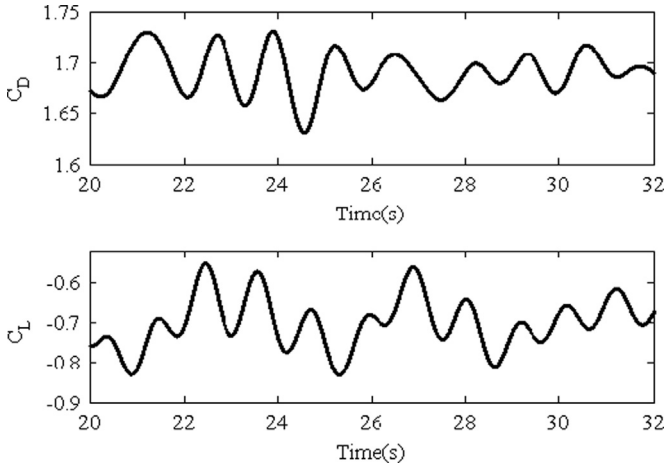

Fig. 3. Drag and lift coefficients as functions of time. The validation simulation is conducted at $Re=2.02\times10^4$, $h^*=4$, and $h_b/s=2.33$.

$St=fL/U_\infty$, is the dimensionless number utilized in the flow characterization of oscillating flow mechanics, where f is the vortex shedding frequency.

Open channel flow, such as rivers and spillways, involve the existence of a free surface between air and water. In these cases, the free surface behavior becomes important. The flow is governed by the forces of gravity and inertia and it can be characterized by the dimensionless parameter, Froude number, $Fr=U_\infty/\sqrt{gd}$ where d is the distance between free surface and the plate tip. The Froude number based on d basically represents the local Froude number and is suitable to characterize the effect of the free surface on the physics of flows near the submerged object (Sheridan et al., 1997).

The schematic of the flow geometry is shown in Fig. 1. Two-dimensional URANS VOF simulations are conducted at $Re=50{,}000$. The entire fluid domain is divided into two parts: water at the bottom and air on the top. The upstream water velocity is set to $U_\infty=0.5$ m/s and the air velocity is set to $U_{air}=0.01$ m/s. The plate height is L. The plate is placed perpendicular to the upstream flow inside a flow channel, which is a simple duct with a height of $16L$. The channel is large enough to eliminate the boundary effects from side walls. The coordinate origin is located at the plate center. The inlet is $20L$ upstream the plate to assure fully developed flow and the outlet is $20L$ downstream the plate to obtain wake dynamics free of outlet effects. The depth to length ratio is $d^*=d/L$. Simulations are conducted for d^* of 7.5, 0.6, 0.5, 0.45, and 0.3. The corresponding local Froude numbers calculated based on depths of plate are 0.18, 0.65, 0.71, 0.75, and 0.92. The property ratios between air and water for all the simulations presented in this manuscript are described as $\rho_1/\rho_2=1.23\times10^{-3}$, $U_{air}/U_\infty=2.00\times10^{-2}$, and $\mu_1/\mu_2=1.82\times10^{-2}$. Modeling the flow past a plate normal to oncoming flow is achieved using ANSYS 14.5

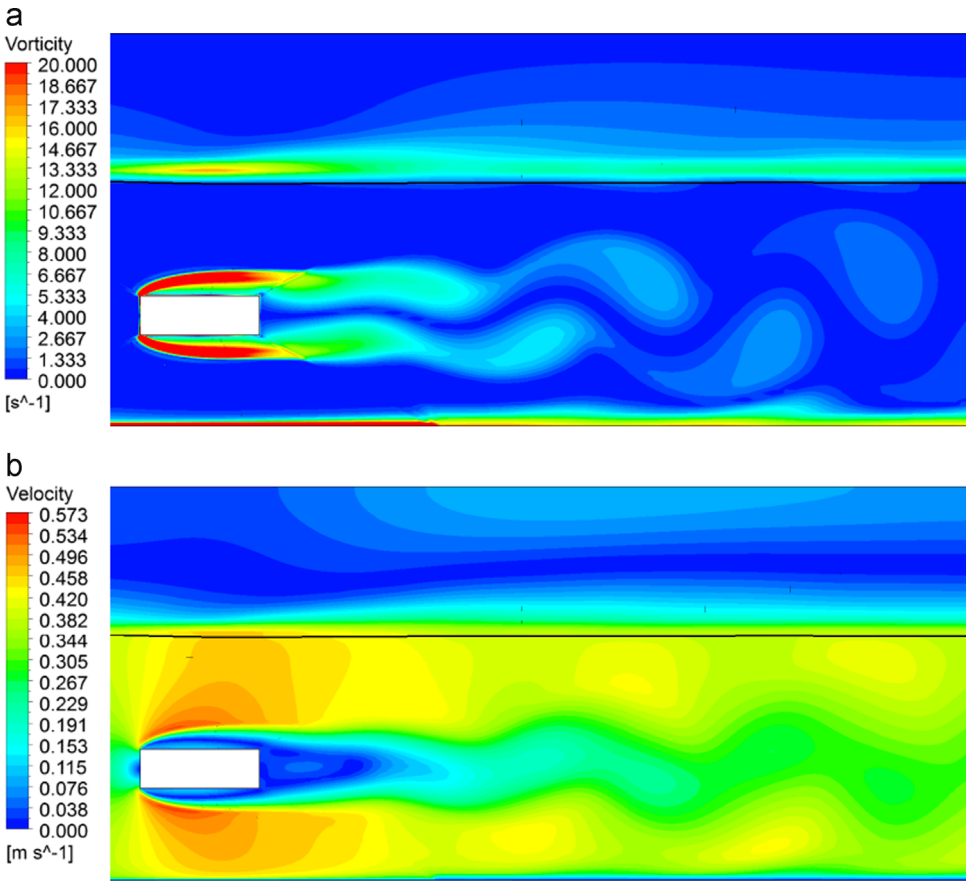

Fig. 4. Instantaneous (a) vorticity and (b) velocity contours at $t=30.3$ s. Validation simulation is conducted at $Re=2.02\times10^4$, $h^*=4$, and $h_b/s=2.33$.

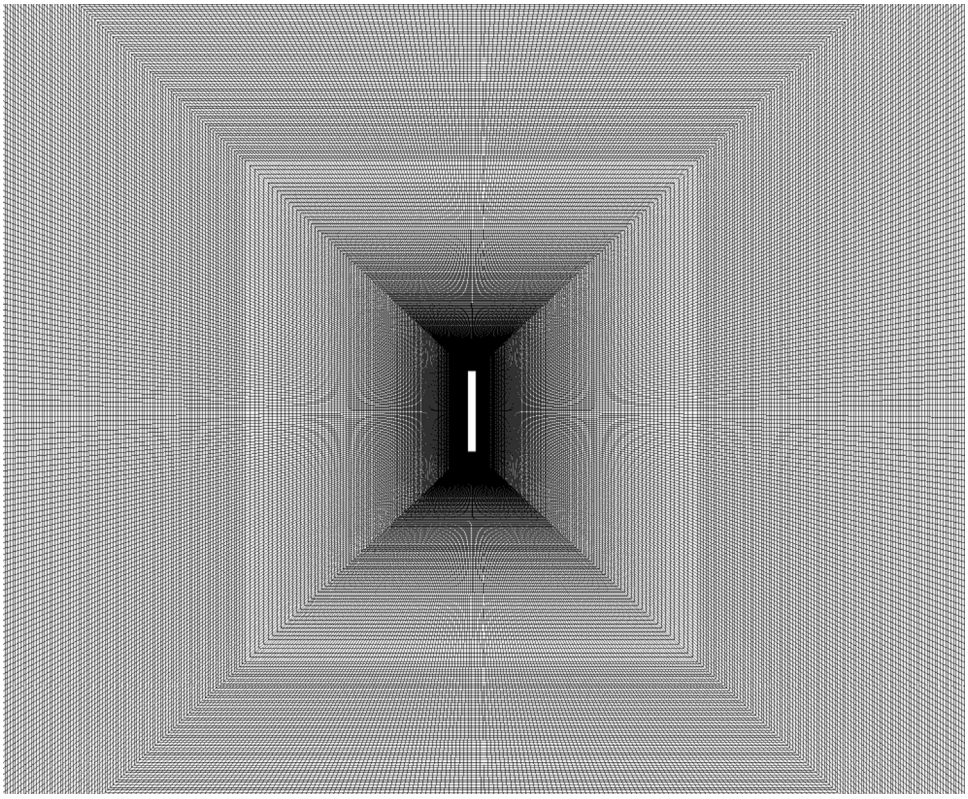

Fig. 5. Structured mesh in the vicinity of the plate.

Fluent simulation tool (see ANSYS theory guide, 2011; ANSYS user guide, 2011). Table 1 listed all the parameter values used in the simulations.

The combination of two separate models is required when modeling flows of two fluids separated by a free surface. Turbulence is modeled with the k–ω SST model (Menter, 1994) and the VOF multiphase model (Hirt and Nichols, 1981 and Monaghan, 1994) is used to determine interface dynamics separating water from air. In order to examine the free surface effect, the VOF model is necessary to track where the air–water interface is located. The k–ω model is an effective turbulence model in predicting flow separation. The two equation k-ω model solves for the turbulence kinetic energy and the specific dissipation rate. The k–ω SST model has been formulated to avoid the upstream sensitivity of the standard k–ω model by combining the advantages of the k–ω model and k–ε model. The equations for turbulent kinetic energy and specific dissipation rate are written in the following form (Menter, 1993, 1994; Wilcox, 2006):

$$\frac{\partial k}{\partial t}+u_j\frac{\partial k}{\partial x_j}=\tau_{ij}\frac{\partial u_i}{\partial x_j}-\beta^* k\omega+\frac{\partial}{\partial x_j}\left[(\nu+\sigma_k\nu_T)\frac{\partial k}{\partial x_j}\right] \tag{7}$$

$$\frac{\partial \omega}{\partial t}+u_j\frac{\partial \omega}{\partial x_j}=aS^2-\beta\omega^2+\frac{\partial}{\partial x_j}\left[(\nu+\sigma_\omega\nu_T)\frac{\partial \omega}{\partial x_j}\right]+2(1-F_1)\sigma_{\omega 2}\frac{1}{\omega}\frac{\partial k}{\partial x_i}\frac{\partial \omega}{\partial x_i} \tag{8}$$

The eddy viscosity and the extra stress tensor are defined as

$$\nu_T=\frac{a_1 k}{\max(a_1\omega,\ \Omega F_2)} \tag{9}$$

$$\tau_{ij}=\nu_T\left(\frac{\partial u_i}{\partial x_j}+\frac{\partial u_j}{\partial x_i}-\frac{2}{3}\frac{\partial u_k}{\partial x_k}\delta_{ij}\right)-\frac{2}{3}k\delta_{ij} \tag{10}$$

Here, Ω is the vorticity magnitude, $a, a_1,\ \beta,\ \beta^*, \sigma_k, \sigma_\omega$, and σ_{ω_2} are closure coefficients, ν is the kinematic viscosity, k is the turbulent kinetic energy, ω is the specific dissipation rate, u_j is the velocity, S is the mean rate-of-strain tensor, and F_1, F_2 are the blending functions. Details of the closure parameters can be found in Menter (1994). Recently, this turbulence model is successfully employed by the present authors to characterize turbulent flow structures near micro-hydro turbines (Schleicher et al., 2013, 2014a, 2014b, 2015).

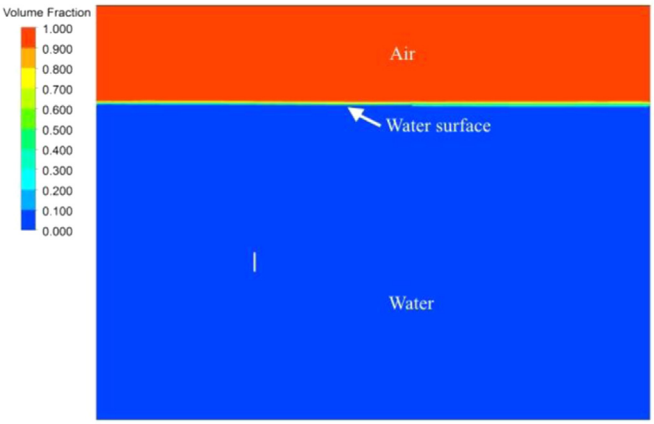

Fig. 6. Volume fraction contour predicted by multiphase simulation.

The VOF model can depict two or more fluids by solving a single set of momentum equations and tracking the volume fraction of each fluid throughout the domain. The implicit scheme is used for time discretization for obtaining the face fluxes for all cells as follows:

$$\frac{\alpha_1^{n+1}\rho_1^{n+1}-\alpha_1^n\rho_1^n}{\Delta t}\forall_{cell}+\sum_f\left(\rho_1^{n+1}U_f^{n+1}\alpha_{1f}^{n+1}\right)=(\dot{m}_{21}-\dot{m}_{12})\forall_{cell} \tag{11}$$

where $n+1$ denotes the index for current time step while n

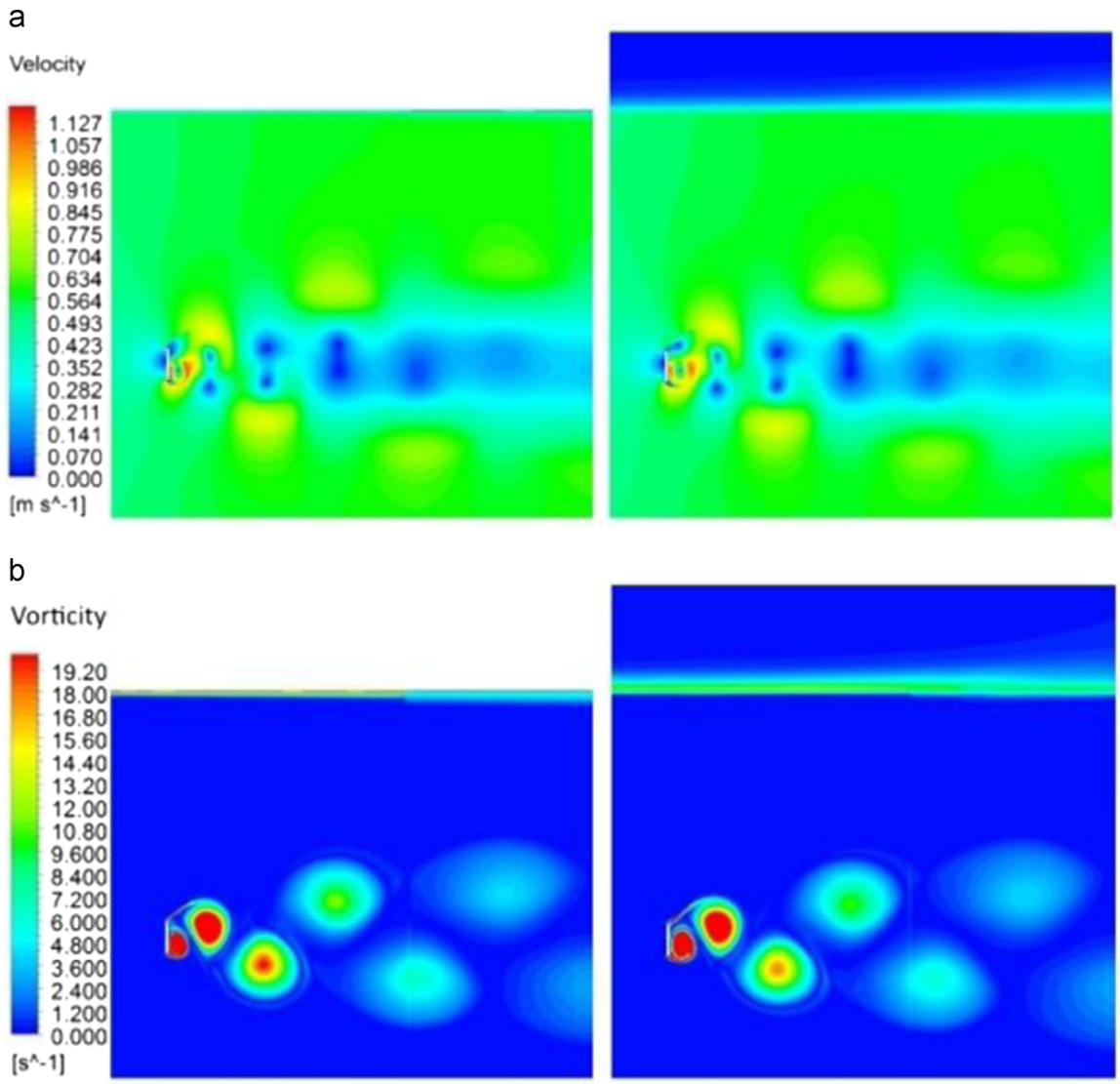

Fig. 7. Instantaneous (a) velocity and (b) vorticity contours. Results of single-phase simulation are shown in the left column and the results of multiphase simulation are shown in the right column.

denotes the index for previous time step. α_{1f} is the face value of the air volume fraction, and U_f is the volume flux through the face based on normal velocity.

The boundary conditions for the simulations are as follows. The mass flow rates for both water and air are specified at the inlet. The computational domain behind the plate is large enough so zero gauge pressure is imposed at the outlet. At the inlet and the outlet, the free surface levels are defined in the VOF model based on the plate depth. A no-slip boundary condition is invoked on the plate surfaces and the bottom boundary. Furthermore, a no shear boundary condition is applied at the top boundary of the domain.

The semi-implicit method for pressure-linked equations (SIMPLE) solution method was used to resolve the coupling between the pressure and the velocity fields. Discretization of time, momentum, turbulent kinetic energy and specific dissipation rate were accomplished through the second-order upwind scheme. The modified high resolution interface capturing (HRIC) discretization scheme was used to solve the volume fraction equation. The transient simulation was stopped after the solution reached periodic stability.

3. Validation

In order to verify the accuracy of the multiphase simulation, a validation test is conducted. Malavasi and Guadagnini (2007) provide experimental data of a rectangular cylinder in the free surface flow. The transient three-dimensional validation simulation is to simulate one of the cases presented in the reference. The schematic of the geometry is shown in Fig. 2. The channel is 5 m long with a cross-section width $B=0.5$ m. The rectangular cylinder is fully submerged in water and the depth is represented as h^*, where $h^*=(h-h_b)/s$. Values of parameters used in the simulation are listed in Table 2. The case with the Reynolds number of 2.02×10^4, $h^*=4$, and the ratio $h_b/s=2.33$ is chosen to be modeled.

Fig. 3 depicts the drag and lift coefficients as functions of time. The mean value of the drag and the lift coefficient, and the Strouhal number observed from validation simulation are 1.69, −0.67, and 0.17, respectively. These values are determined from the time signature of the drag and the lift coefficient at flow time 24–32 s in order to avoid the initial transient effects. Predicted results from the present study have relative errors of less than 6% when compared with the drag and the lift coefficients and the

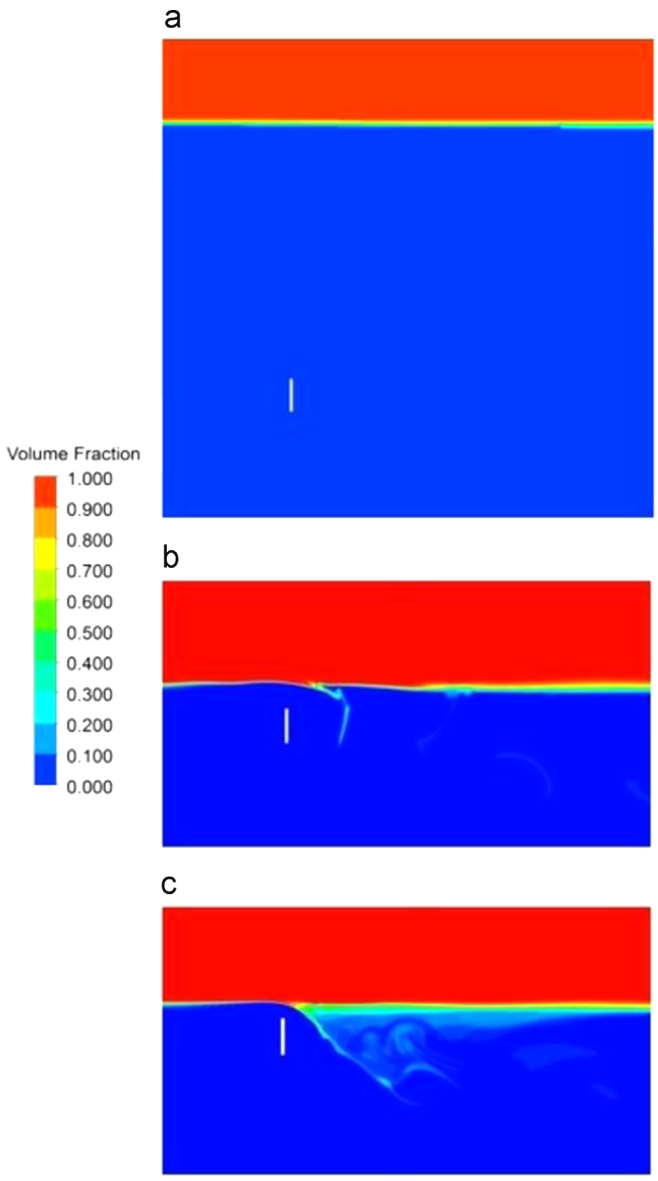

Fig. 8. Instantaneous volume fraction contour for (a) $Fr=0.18$ at $t=26.4$ s, (b) $Fr=0.65$ at t=28.8 s and (c) $Fr=0.92$ at $t=28$ s.

Strouhal number documented by Malavasi and Guadagnini (2007). Fig. 4 depicts an instantaneous velocity and vorticity contours for flow time 30.3 s. The black horizontal line above the rectangular cylinder indicates the free surface location, which is slightly perturbed from its resting state.

4. Mesh optimization and temporal convergence

The VOF model is susceptible to instabilities if non-orthogonal elements exist in the discretized fluid mesh. Therefore, the mesh used for the multiphase simulations must be carefully chosen to allow for acceptable accuracy as well as numerical stability. Increasing the number of cells in the mesh may produce more accurate simulation results; however, a higher mesh density results in a substantially longer computational time and increased CPU usage.

A spatial convergence test is conducted in order to assess the numerical accuracy of the simulations. The grid size used in this paper is verified using the Richardson extrapolation based grid convergence method (GCI method) given in Celik et al. (2008). This procedure is used to estimate the numerical uncertainty and error due to discretization in Computational fluid dynamics (CFD) studies. The methodology of this procedure is first to define a representative cell size. Second, select three significantly different grid sets $N_1=$ 90,620 cells, $N_2=$ 158,200 cells, and $N_3=$ 282,050 cells. The grids are selected to make sure the refinement factors $r_1=h_1/h_2$ and $r_2=h_2/h_3$ are greater than 1.3, where $h_i=\left[\frac{1}{N_i}\sum_{j=1}^{N_i}(\Delta A_j)\right]^{\frac{1}{2}}$ is the representative cell size for the ith grid. The drag coefficient value is determined as the key variable of each grid. The grid convergence index (GCI value) is calculated to estimate discretization errors between grids. The GCI value for the finer grid should be relatively small to show that the solution can be replicated when the finest grid is employed. In the present study, the GCI value between meshes N_1 and N_2 is 2.9% and the value between meshes N_2 and N_3 is 1.1%. This indicated that the mesh size used in the study, N_3, provides results that can be considered mesh independent. The detailed description of the method is presented by Celik et al. (2008).

A structured, hexahedral mesh was used for the computations. The mesh is finer closer to the plate walls and downstream of the plate to resolve the boundary layer and to observe vortex shedding. Fig. 5 depicts the mesh in the vicinity of the plate.

Discrete time steps are used in transient simulations. The sensitivity of the simulation results to the time step size must be examined to accurately capture the unsteady flow field. A temporal convergence test is conducted for the case of plate depth equal to 0.6 L. Drag coefficients are determined for three time step sizes $\Delta t=0.008$ s, 0.0016 s, and 0.00032 s with corresponding values of 3.32, 3.55, and 3.55. This shows that $\Delta t=0.0016$ s is sufficient to ensure the temporal convergence.

A non-dimensional wall distance in a wall-bounded flow is defined as $y^+=u_* y/\nu$, where u_* is the friction velocity at the nearest wall and y is the distance to the nearest wall. The average y^+ values at the plate wall for cases of $Fr=0.18$, 0.65, 0.71, 0.75, and 0.92 are 4.76, 3.31, 2.81, 2.57, and 1.80, respectively. The y^+ values are all below 5, ensuring that the viscous sublayer is numerically resolved. The Courant number ($C=u\Delta t/\Delta x$) is a non-dimensional parameter that describes how fast flow information is propagated through the computational domain. The Courant–Friedrichs–Lewy (CFL) condition is a numerical stability criterion that requires $C\leq 1$ for a stable, unsteady solution. The average values of the Courant number for all plate depths cases are all below unity. The maximum value of the local Courant number is 46.2, which occurs at a few cells near the top and the bottom plate corners.

5. Results and discussion

For additional validation of the model, results predicted by the multiphase model are compared to those predicted by the single-phase model. The single-phase simulation considers the flow past a plate in a nearly infinite fluid domain. In order to make the boundary conditions in multiphase simulation similar to the single-phase simulation, the plate is fully submerged in the channel and oriented at a distance of approximately 7.5L away from the water surface. The volume fraction contour of multiphase simulation is illustrated in Fig. 6. As shown in Fig. 6, the water depth of the multiphase simulation is set to be the same as the channel height in the single-phase simulation. Fig. 6 shows no disturbances at the water surface, which suggests that the flow field near the plate is not influenced by the presence of the free

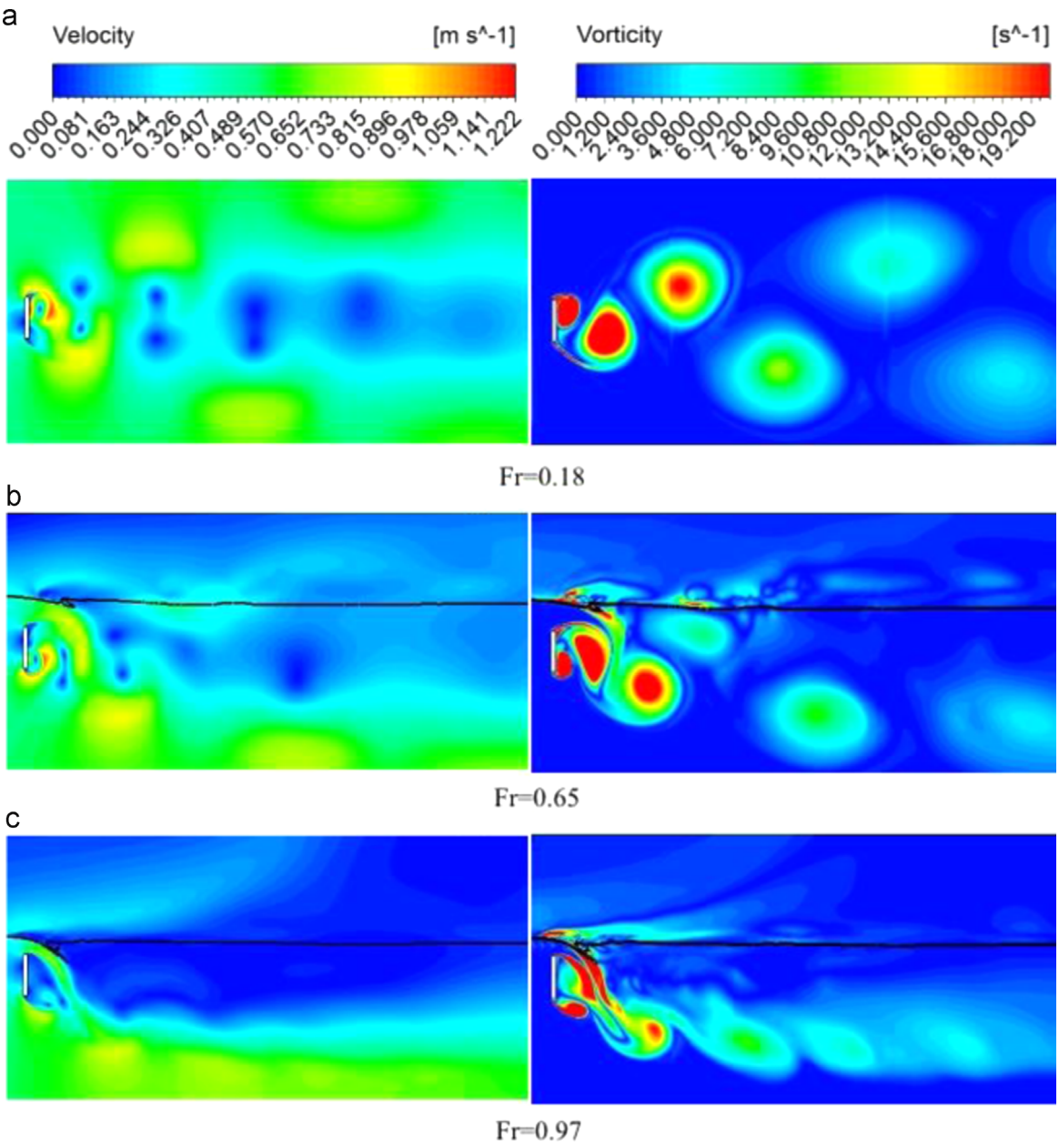

Fig. 9. Instantaneous velocity and vorticity contours for (a) $Fr=0.18$ at $t=26.4$ s, (b) $Fr=0.65$ at $t=28.8$ s and (c) $Fr=0.92$ at $t=28$ s.

surface. Therefore, the results for the multiphase simulation should be identical with the single-phase simulation.

Fig. 7 depicts the same velocity and vorticity distribution for both single-phase and multiphase simulations. Fig. 7(b) shows that the vortices shed from both the top and bottom surfaces of the plate interact with one another, which then gradually dissipate downstream. The vortices are shed alternatively from the top and the bottom corner of the plate and generate a regular flow pattern in the wake. Other than the volume fraction and the vorticity contour, the mean drag coefficient and the Strouhal number are calculated from at least ten vortex shedding cycles. As reported by many earlier investigators such as Tamura et al. (1990); Mittal and Balachandar (1995); Najjar and Vanka (1995); Bosch and Rodi (1998); Najjar and Balachandar (1998); and Tian et al. (2013), the two-dimensional flow simulation over-predicts the drag coefficients. Najjar and Balachandar (1998) compared the numerical results for two-dimensional and three-dimensional simulations, indicating that the three-dimensional effect is the reason for the over-prediction of the two-dimensional simulations. The present study is in agreement with the two-dimensional numerical results reported in the literature. The drag coefficient value and the Strouhal number for the single-phase simulation are 3.86 and 0.125, while the same values predicted by the multi-phase simulation are 3.86 and 0.126, respectively. Results show that the single-phase and multiphase simulations yield identical values for desired performance characteristics regardless of the use of multiphase VOF model when the plate is sufficiently far away from the free surface.

Investigating the free surface effects was the primary focus of this manuscript. As previously mentioned, the three-dimensional validation simulation was conducted to assure the accuracy of the mathematical model and the numerical method; however, two-dimensional simulations were conducted because three-dimensional simulations were too computationally expensive for the time allotted for this study. It is observed that the proximity of the plate to the surface has a profound effect on the spatial and temporal characteristics of the

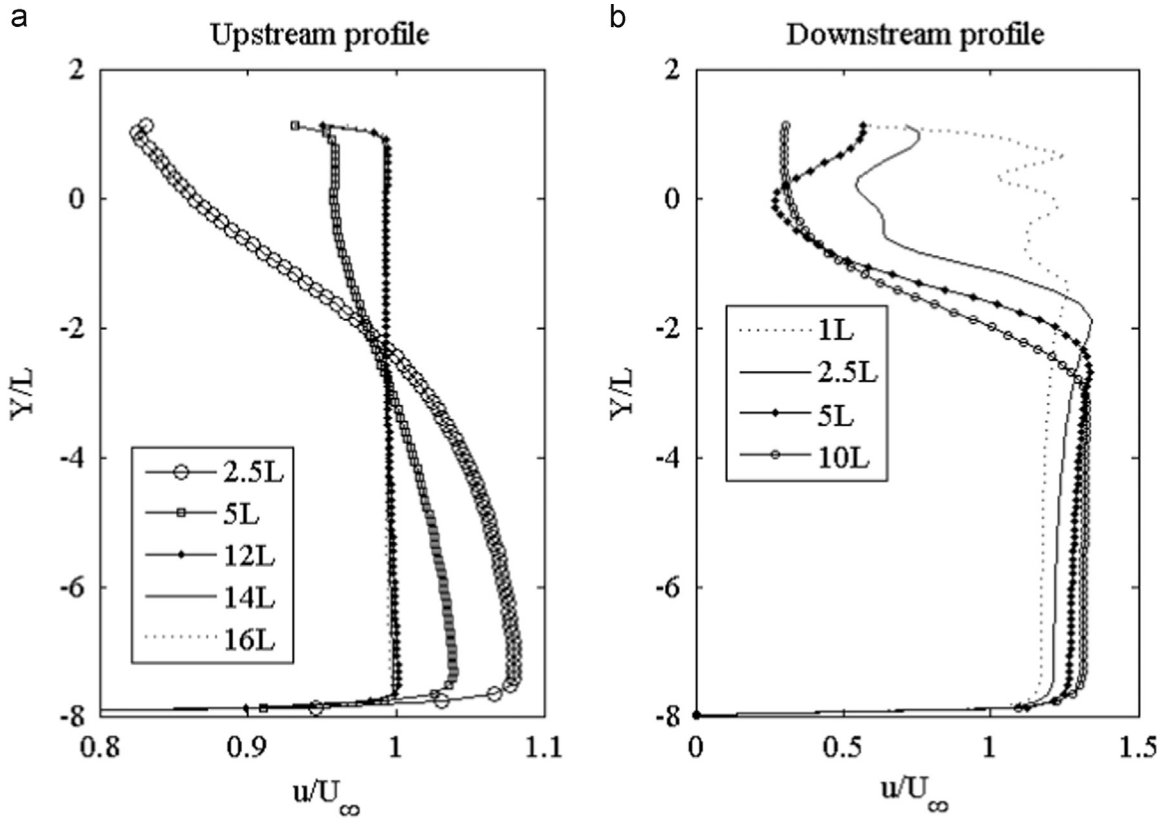

Fig. 10. Normalized profiles of the time averaged streamwise component of velocity for $Fr=0.65$ at various locations (a) upstream and (b) downstream of the plate.

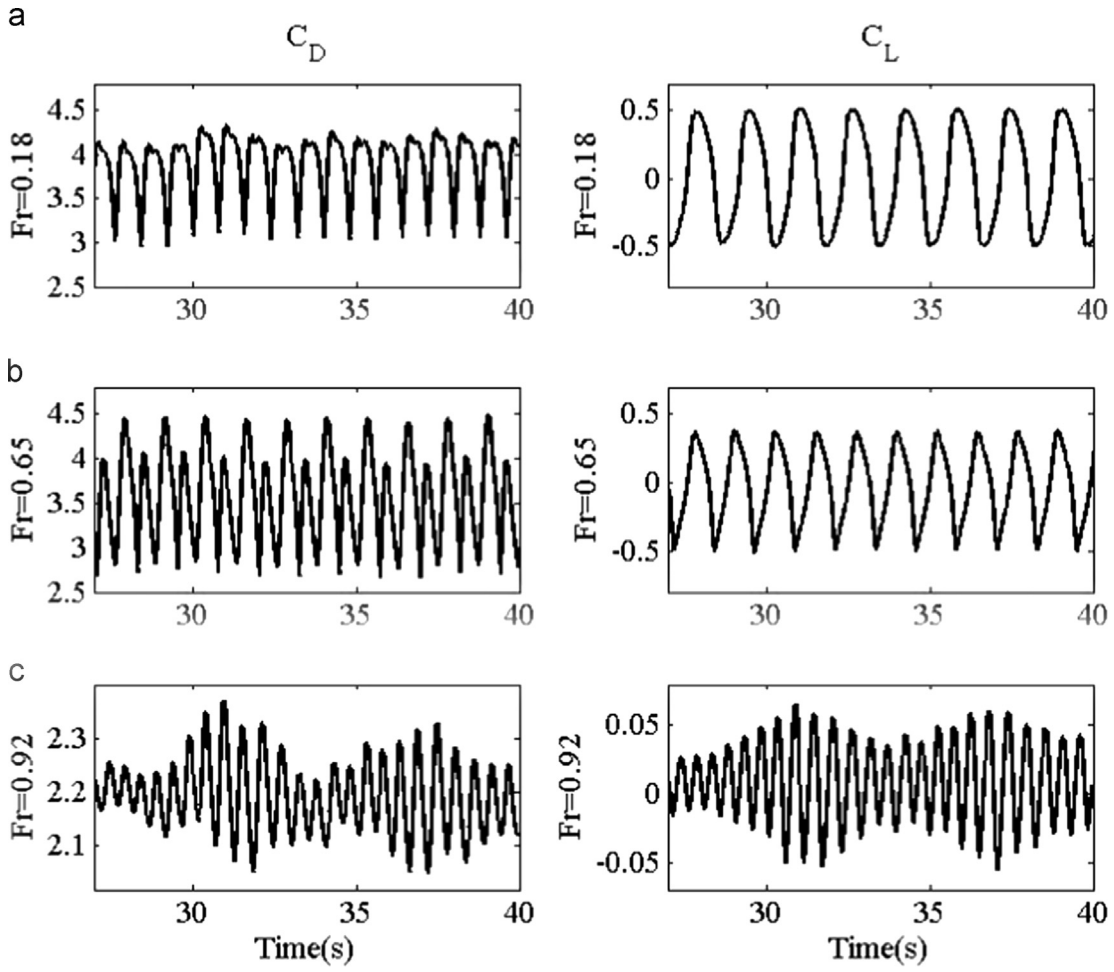

Fig. 11. Drag and lift coefficients as functions of time for (a) $Fr=0.18$ (b) $Fr=0.65$ and (c) $Fr=0.92$.

vorticity and velocity field. The wake structure is distinctly different from the deeply submerged plate.

Fig. 8 shows the instantaneous volume fraction contour at different plate depths. The volume fraction contour depicts the local air and water fraction, where zero represents pure water and one represents pure air. When the plate is submerged to 7.5L (Fr=0.18), no surface deformation is observed. When the plate is 0.6L submerged (Fr=0.65), some surface deformation is observed. The flow above the plate interacts with the surface, resulting in a drop in the surface right behind the plate. The surface wave decays in magnitude far downstream of the plate. When the plate is submerged to 0.3L (Fr=0.92), additional fluctuation along the surface is observed. As depicted in Fig. 8(c), more air is entrained into the water region behind the plate and results in larger surface distortion.

The present study observes similar flow features as depicted in Miyata et al. (1990) and Sheridan et al. (1997). Fig. 9 illustrates the velocity and vorticity contour for different values of the Froude number. The black horizontal line above the plate shown in Fig. 9 (b) and (c) indicates the free surface location. The free surface penetrates into the plate's near wake as the Froude number becomes larger. Vortex shedding alternating from upper and lower plate boundary is observed in all cases. The vorticity contour shows that the free surface has a drastic effect on the flow. The vortex shedding is symmetric and regular for Fr=0.18 as seen in Fig. 9(a). For the cases of Fr=0.65 and 0.92 (Fig. 9(b) and (c)), the upper vortex shedding component is influenced by the free surface, resulting in asymmetric vortex shedding and irregular flow pattern in the wake. As shown in Fig. 9(b) for the case of Fr=0.65, the large scale vortex shedding is asymmetric. The upper vortices are dissipated by the free surface and then break into small eddies near the surface, leaving the bottom vortices to dissipate further downstream. When the plate approaches even closer to the surface as shown in Fig. 9(c) for the case of Fr=0.95, a vortex forms above the top of the plate and adjacent to the free surface. A jet-like flow is observed from the free surface on top of the plate. This jet-like flow is dominated by the vortices generated from the free surface, which induce strong free surface deformation. Smaller vortices are seen in this case compared to others. The jet flow tends to merge with the vortices originating from the bottom of the plate. The vortex shedding from top and bottom of the prism are pushed downward due to the presence of the jet-like flow. Moreover, the upper vortices are not only compromised by the free surface, but are also blended together with the bottom vortices and dissipate together downstream and the wake flow becomes even more irregular. Characteristics of the drag and lift coefficients are directly affected by different vortex shedding motions.

Table 3
Mean and root mean square of fluctuating drag and lift coefficients and the Strouhal number for different values of the Froude number.

	Fr=0.18	Fr=0.65	Fr=0.71	Fr=0.75	Fr=0.92
C_D	3.86	3.55	2.75	2.65	2.18
C_{Drms}	0.36	0.51	0.29	0.27	0.07
C_L	0.00	−0.02	−0.04	−0.03	0.01
C_{Lrms}	0.38	0.28	0.17	0.14	0.03
St	0.125	0.162	0.208	0.233	0.355

The profiles of time averaged streamwise component of the velocity at the upstream and the downstream of the plate are shown in Fig. 10 for Fr=0.65. The velocity profiles are averaged over 5 vortex shedding cycles. Upstream velocity profiles are plotted at locations 2.5L, 5L, 12L, 14L, and 16L away from the plate, as depicted in Fig. 10(a). The velocity profiles at about 12L and 14L from the plate are nearly the same, suggesting that the fully developed flow conditions are attained at these locations. The velocity profiles approaching plates (5L and 2.5L) are influenced by the presence of the plate and the free surface. The water speed decreases near the free surface due to the slower air velocity above. Downstream velocity profiles are plotted 1L, 2.5L, 5L, and 10L away from the plate, as depicted in Fig. 10(b). Irregular flow pattern caused by the interaction of the vortices shed by the plate and the free surface effects in near wake velocity profiles is shown at 1L and 2.5L away from the plate. Further away from the plate at 5L and 10L the velocity profiles gradually recover to regular wake flow patterns.

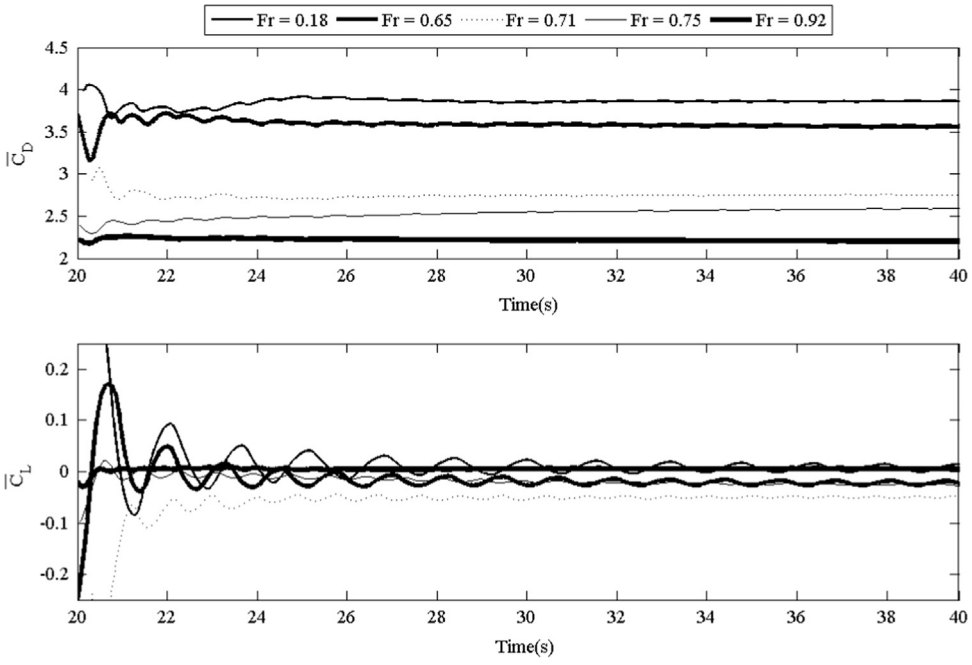

Fig. 12. Cumulative mean of drag and lift coefficients for Fr=0.18, 0.65, 0.71, 0.75 and 0.92.

Fig. 11 shows the drag and the lift coefficient as functions of time for various values of the Froude number. The mean values of the force coefficients are calculated when the periodic state is reached. Mean values are determined from the time signature of drag and the lift coefficient at flow time between 30 s and 40 s which spans nearly 6 vortex shedding cycles. It is seen that the drag coefficient (C_D) has a mean value of 3.86 in the case of $Fr=0.18$ (where the plate is far away from the surface). In the case of $Fr=0.65$, C_D decreases to 3.55. By further decreasing the submergence depth to the case of $Fr=0.92$, C_D reduces to 2.18, corresponding to a 38% drop relative to the case of $Fr=0.65$. Results show that the influence of the free surface is significant when the plate approaches the free surface. The different vortex shedding motion effects are revealed when investigating the variation for both drag and lift coefficients. The drag and the lift coefficients display periodic behavior for all cases. When the plate is far away from the free surface (see Fig. 11(a)), the vortex shedding in this case is symmetric and very regular. When the plate is near the free surface (see Fig. 11(b) and (c)), the drag and lift coefficients have more complicated dynamics with several modes present. In Fig. 11 (c), the variation of the force coefficients shows that multiple wave motions are combined due to the domination of the jet-like flow formed from the free surface. Table 3 lists the mean and the root mean square (rms) of fluctuating force coefficients and the Strouhal number determined for various values of *Fr*. The drag coefficient decreases from 3.86 ($Fr=0.18$) to 3.55 ($Fr=0.65$) and then rapidly drops to 2.75 at $Fr=0.71$. The drag coefficient does not change as much as *Fr* increases from 0.71 to 0.75, while it decreases substantially to 2.18 as *Fr* is increased to 0.92. The rms of C_D fluctuation at first increases to 0.51 ($Fr=0.65$) and then drops significantly to 0.29 ($Fr=0.71$). Another significant drop from 0.27 ($Fr=0.75$) to 0.07 ($Fr=0.92$) is also obtained. Past studies of flow past a circular cylinder have reported a reduction in drag coefficient and an increase in the Strouhal number when reducing the gap ratio between the cylinder and the free surface. The Strouhal number increases from 0.162 ($Fr=0.65$) to 0.355 ($Fr=0.92$), and simultaneously the rms of fluctuating lift force decreases. The change of vortex shedding frequency is closely related to the substantial decrease of drag coefficient. Furthermore, the lift coefficient shows that there are several modes of flow transitions dominating the flow. This implies that the vortex shedding at shallow depths is not governed by a single mode in comparison when the prism is submerged in a nearly infinite flow domain.

The cumulative mean of drag and lift coefficient as a function of time is shown in Fig. 12 for various values of *Fr*. The mean of force coefficients is calculated starting at 20 s by using the instantaneous data at every 0.0016 s. The cumulative mean values tend to constant asymptotically, implying that the force coefficients have reached stability. The mean values of the force coefficient listed in Table 3 have relative error less than 5% when compared to the asymptotic values of the cumulative mean of force coefficients. This discrepancy is due to the fact that initial transient at early simulation time influences the overall cumulative mean values. As simulations are carried out further in time this difference naturally becomes smaller.

To determine the cause of the drag coefficient reduction, a simulation was conducted with a solid surface (no-slip surface) replacing the free surface. The solid surface is placed 0.5*L* away from the top of the plate, this case would correspond to $Fr=0.71$ if the free surface is present. The mean value of the drag coefficient is calculated to be 3.67 with the solid surface, which is much closer to the value of the drag coefficient, 3.86, for a plate in an infinite domain. As presented above the drag coefficient is 2.75 for $Fr=0.71$. It can be concluded that the reduction in drag coefficient is not simply by the confinement. The interaction of the free surface waves and the wake flow should be the reason for drag reduction. This does not rule out the possibility of the adverse influence of the air entrainment deep into the wake, as seen in Fig. 8.

6. Conclusions

Numerical simulations were performed to understand the flow structure about a plate placed near the free surface. The free surface effect on the plate was investigated by performing simulations at 7.5*L*, 0.6*L*, 0.5*L*, 0.45*L*, and 0.3*L* depths corresponding to local Froude number values of 0.18, 0.65, 0.71, 0.75, and 0.92. Two-dimensional transient simulations were conducted for the Reynolds number of 50,000. The k–ω SST turbulence model and VOF multiphase model were employed with a transient SIMPLE solver to solve flow past a plate close to the free surface. A three-dimensional validation simulation was conducted to compare with a previously published experimental result presented in Malavasi and Guadagnini (2007). The results for both drag and lift coefficients and the Strouhal number match well with their results. Simulation accuracy is verified by performing spatial and temporal discretization convergence tests, providing a GCI value of 1.1% on drag coefficient for a 282,050 cell mesh and time step size of $\Delta t=0.0016$ s.

The presented results showed that as the depth decreased from 0.6*L* (i.e., $Fr=0.65$) to 0.3*L* (i.e., $Fr=0.92$), the drag coefficient decreased 38% from 3.55 to 2.18. The Strouhal number increased from 0.162 to 0.355. The substantial changes observed are similar to flow past a circular cylinder close to the free surface. The variation of drag coefficient with depth was consistent with the results reported in Miyata et al. (1990). The flow pattern observed is also consistent with the results in Sheridan et al. (1997) and Reichl et al. (2005). The wake structure for a near-surface plate is distinctly different from the wake of a deeply submerged plate. The wake flow becomes more irregular as depth decreases. The vortex formed from the top of the plate break into small eddies due to the presence of the free surface. Furthermore, a jet-like flow formed from the surface on top of the plate was observed, which weakened the upper vortices and results in large surface deformation. The presented study demonstrates that the proximity of the blades to the free surface has profound influence on the energy harvesting devices performance in the river or ocean currents. The rapid decrease in drag coefficient occurs between a depth of 0.6*L* ($Fr=0.65$) and 0.5*L* ($Fr=0.71$) at the flow conditions considered, therefore, the plate depths greater than 0.6*L* are suggested for the energy harvesting devices utilizing rectangular prism shape blades.

Acknowledgment

The authors would like to gratefully acknowledge funding from the Office of Naval Research, United States for this work under Award N00012-14-C-0078 through a SBIR grant with e-Harvest.

References

ANSYS FLUENT Theory Guide Release 14.5, 2011.
ANSYS FLUENT User Guide Release 14.5, 2011.
Arslan, T., Malavasi, S., Pettersen, B., Andersson, H.I., 2013. Turbulent flow around a semi-submerged rectangular cylinder. J. Offshore Mech. Arct. Eng. 135, 4.
Bayraktar, S., Yayla, S., Oztekin, A., Ma, H.L., 2014. Wall proximity effects on flow over cylinders with different cross sections. Can. J. Phys. 92 (10), 1141–1148.
Bosch, G., Rodi, W., 1998. Simulation of vortex shedding past a square cylinder with different turbulence models. Int. J. Numer. Methods Fluids 28 (4), 601–616.
Celik, I., Ghia, U., Roache, P., Christopher, 2008. Procedure for estimation and reporting of uncertainty due to discretization in CFD applications. J. Fluids Eng. 130, 7.

Fage, A., Johansen, F.C., 1927. On the flow of air behind an inclined flat plate of infinite span. Proc. R. Soc. A: Math. Phys. Eng. Sci. 116 (773), 170–197.
Hirt, C.W., Nichols, B.D., 1981. Volume of fluid (VOF) method for the dynamics of free boundaries. J. Comput. Phys. 39 (1), 201–225.
Knisely, C.W., 1990. Strouhal numbers of rectangular cylinders at incidence: a review and new data. J. Fluids Struct. 4 (4), 371–393.
Malavasi, S., Guadagnini, A., 2007. Interactions between a rectangular cylinder and a free-surface flow. J. Fluids Struct. 23 (8), 1137–1148.
Menter, F.R., 1993. Zonal two equation k–ω turbulence models for aerodynamic flows. In: Proceedings of 24th Fluid Dynamics Conference, AIAA.
Menter, F.R., 1994. Two-equation eddy-viscosity turbulence models for engineering applications. AIAA J. 32 (8), 1598–1605.
Mittal, R., Balachandar, S., 1995. Effect of three-dimensionality on the lift and drag of nominally two-dimensional cylinders. Phys. Fluids (1994) 7 (8), 1841–1865.
Miyata, H., Shikazono, N., Kanai, M., 1990. Forces on a circular cylinder advancing steadily beneath the free-surface. Ocean Eng. 17 (1–2), 81–104.
Monaghan, J.J., 1994. Simulating free surface flows with SPH. J. Comput. Phys. 110 (2), 399–406.
Najjar, F.M., Balachandar, S., 1998. Low-frequency unsteadiness in the wake of a normal flat plate. J. Fluid Mech. 370, 101–147.
Najjar, F.M., Vanka, S.P., 1995. Simulations of the unsteady separated flow past a normal flat-plate. Int. J. Numer. Methods Fluids 21 (7), 525–547.
Narasimhamurthy, V.D., Andersson, H.I., 2009. Numerical simulation of the turbulent wake behind a normal flat plate. Int. J. Heat. Fluid Flow. 30 (6), 1037–1043.
Negri, M., Cozzi, F., Malavasi, S., 2010. Self-synchronized phase averaging of PIV measurements in the base region of a rectangular cylinder. Meccanica 46 (2), 423–435.
Reichl, P., Hourigan, K., Thompson, M.C., 2005. Flow past a cylinder close to a free surface. J. Fluid Mech. 533 (00), 269–296.
Schleicher, W., Ma, H., Riglin, J., Kraybill, Z., Wei, W., Klein, R., Oztekin, A., 2014a. Characteristics of a micro-hydro turbine. J. Renew. Sustain. Energy 6 (1), 1–14.
Schleicher, W.C., Riglin, J.D., Kraybill, Z.A., Oztekin, A., 2013. Design and simulation of a micro hydrokinetic turbine. 1st Marine Energy Technology Symposium, Washington, D.C.
Schleicher, W.C., Riglin, J.D., Oztekin, A., 2015b. Numerical characterization of a preliminary portable micro-hydrokinetic turbine rotor design. Renew. Energy. 76, 234–241. http://dx.doi.org/10.1016/j.renene2014.11.032.
Schleicher, W.C., Riglin, J.D., Oztekin, A., Klein, R.C., 2014b. Numerical Optimization of a Portible Hydrokinetic Turbine 2014b. In: Proceedings of 2nd Marine Energy Technology Symposium, Seattle, WA.
Sheridan, J., Lin, J.C., Rockwell, D., 1997. Flow past a cylinder close to a free surface. J. Fluid Mech. 330, 1–30.
Tamura, T., Ohta, I., Kuwahara, K., 1990. On the reliability of two-dimensional simulation for unsteady flows around a cylinder-type structure. J. Wind. Eng. Ind. Aerodyn. 35 (0), 275–298.
Tian, X., Ong, M.C., Yang, J., Myrhaug, D., 2013. Unsteady RANS simulations of flow around rectangular cylinders with different aspect ratios. Ocean Eng. 58 (0), 208–216.
Wilcox, D.C., 2006. Turbulence modeling for CFD, 3rd ed. DCW Industries, La Cānada, Calif.